Data-driven Fuzzy Weights-of-Evidence model for identification of potential zeolite-bearing environments on Mars.

Gayantha Roshana Loku Kodikara[1] and Lindsay Jean McHenry[2]

[1]University of Wisconsin Milwaukee
[2]University of Wisconsin-Milwaukee

November 28, 2022

Abstract

The evolution of the climate and hydrochemistry of Mars is still a mystery but it must have been at least occasionally warm and wet to have formed the ancient fluvial and lacustrine landforms observed today. Terrestrial examples and geochemical modeling under proposed early Mars conditions show that zeolite minerals are likely to have formed under alkaline (pH > 8) conditions with low water/rock ratio and surface temperatures below 150 °C. The identification and spatial association of zeolites on the surface of Mars could thus be used to reconstruct the paleoclimate, paleohydrochemistry, and geological evolution of some locations on Mars. Previous studies identified the zeolite analcime and discuss the difficulties of identifying other zeolite species on the surface of Mars using orbital spectroscopy. We used published global mineralogical, geological, geomorphological, hydrological, physical, and elemental abundance maps and the locations of hydrous minerals detected and mapped using orbital data to create a map that delineates favorable areas to look for zeolites on Mars. We used the data-driven fuzzy-based weights-of-evidence method to identify and map favorable areas for zeolites on the surface of Mars up to ± 40° latitudes towards the poles. The final map shows that the eastern and western Arabia deposits, some sites in the Medusae Fossae formation, and some areas within and near Valles Marineris, Mawrth Vallis, highlands north of Hellas, and the Terra Cimmeria and Terra Sirenum regions would be favorable areas to look for zeolites using targeted orbital spectral analysis or future in situ observations.

Hosted file

`essoar.10512417.1.docx` available at https://authorea.com/users/557286/articles/606934-data-driven-fuzzy-weights-of-evidence-model-for-identification-of-potential-zeolite-bearing-environments-on-mars

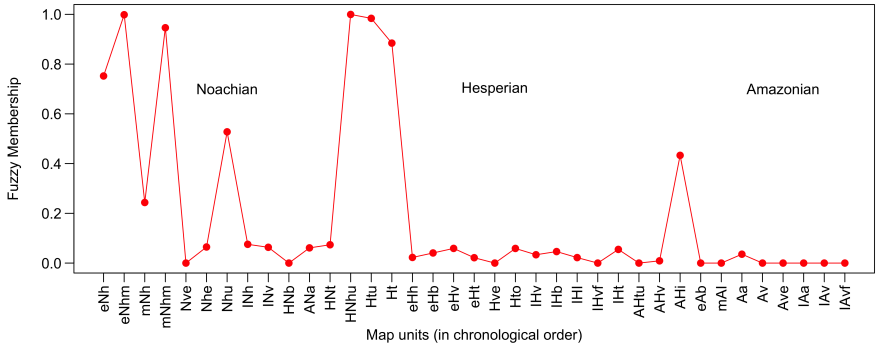

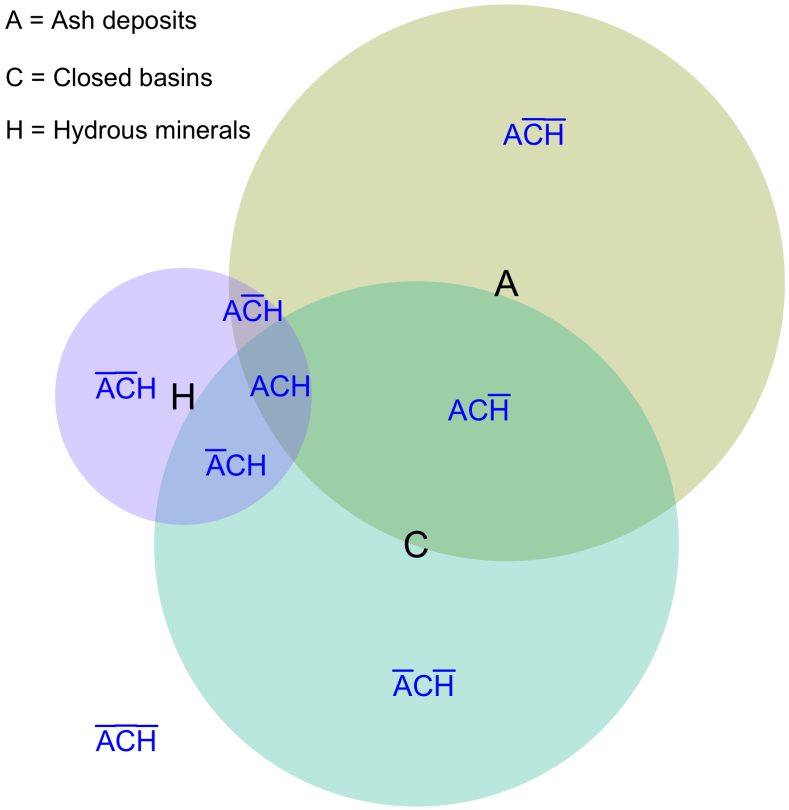

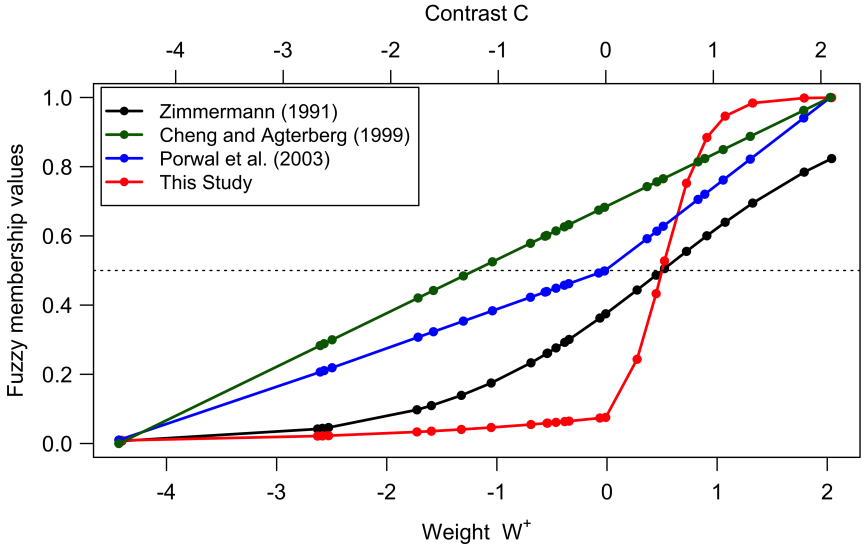

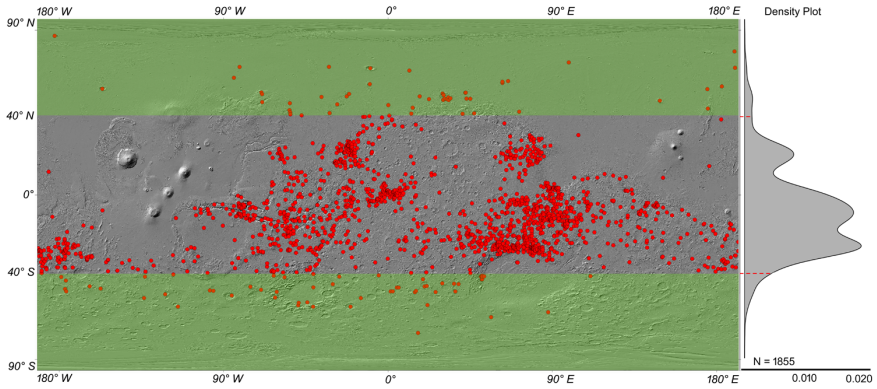

Data-driven Fuzzy Weights-of-Evidence model for identification of potential zeolite-bearing environments on Mars.

Gayantha R. L. Kodikara[1] and Lindsay J. McHenry[1]

[1]Department of Geosciences, University of Wisconsin-Milwaukee, Milwaukee, WI 53211, USA

Corresponding author: Gayantha R. L. Kodikara (gayantha_kodikara@yahoo.com)

Key Points:

- This study creates a map to delineate the favorable areas to look for zeolites on the surface of Mars.
- We used the data-driven fuzzy-based weights-of-evidence method to identify and map favorable areas for zeolites using published global maps on Mars.
- The final map shows the prospective areas for zeolites which could be used to for more detailed orbital data analysis or future in situ observations.

Abstract

The evolution of the climate and hydrochemistry of Mars is still a mystery but it must have been at least occasionally warm and wet to have formed the ancient fluvial and lacustrine landforms observed today. Terrestrial examples and geochemical modeling under proposed early Mars conditions show that zeolite minerals are likely to have formed under alkaline (pH $>$ 8) conditions with low water/rock ratio and surface temperatures below 150 °C. The identification and spatial association of zeolites on the surface of Mars could thus be used to reconstruct the paleoclimate, paleohydrochemistry, and geological evolution of some locations on Mars. Previous studies identified the zeolite analcime and discuss the difficulties of identifying other zeolite species on the surface of Mars using orbital spectroscopy. We used published global mineralogical, geological, geomorphological, hydrological, physical, and elemental abundance maps and the locations of hydrous minerals detected and mapped using orbital data to create a map that delineates favorable areas to look for zeolites on Mars. We used the data-driven fuzzy-based weights-of-evidence method to identify and map favorable areas for zeolites on the surface of Mars up to $\pm$ 40° latitudes towards the poles. The final map shows that the eastern and western Arabia deposits, some sites in the Medusae Fossae formation, and some areas within and near Valles Marineris, Mawrth Vallis, highlands north of Hellas, and the Terra Cimmeria and Terra Sirenum regions would be favorable areas to look for zeolites using targeted orbital spectral analysis or future in situ observations.

Plain Language Summary

Our knowledge of early Mars environmental conditions is limited. Field examples from the Earth and computer models that simulate how zeolites form under

early Martian conditions showed that they prefer water-limited, high pH conditions and surface temperatures below 150 °C. Therefore, if zeolite minerals are present in certain locations on the surface of Mars, based on their presence, we can infer the geological and environmental history of that location. We used a computer model to identify where zeolite minerals can be present on Mars, based on existing maps and data sets of Martian surface features, properties, and compositions. Using that model, we identified several areas of Mars that would have been favorable for zeolites, which could be targeted for future more detailed studies.

1 Introduction

Zeolites are some of the most commonly found authigenic silicate minerals in terrestrial sedimentary deposits (Hay and Sheppard, 2001; Hay, 1966). Zeolite occurrences in sedimentary environments on Earth can be categorized into six groups based on their geologic and hydrologic settings; 1) saline-alkaline lakes (e.g., Lake Tecopa, California; Sheppard and Gude, 1968), 2) soils and land surfaces (e.g., Lake Bogoria basin, Kenya; Renaut, 1993), 3) deep sea sediments (e.g., North-West Pacific; Lee, 1988), 4) open hydrologic systems (e.g. the White River sequence, Wyoming, USA; Lander and Hay, 1993), 5) hydrothermal alteration (e.g., Yucca Mountain, Nevada, USA; Sheppard et al., 1988), and 6) burial diagenesis (e.g., Mogami district, Yamagata, Japan; Iijima, 1988). Overall, zeolites are most abundant in volcaniclastic deposits since volcanic glass is a major zeolite precursor (Hay and Sheppard, 2001). Whether zeolites form and are preserved depends on the thermodynamic equilibrium of fluid-mineral reactions caused by water chemistry (Chipera and Apps, 2001), and kinetically controlled non-equilibrium growth and dissolution reactions (Dibble and Tiller, 1981). Therefore, the presence and nature of zeolites is a good probe to reconstruct the geological and hydrological history of zeolite-bearing environments on Earth (e.g., Chipera and Apps, 2001; McHenry et al., 2020).

Zeolites are also postulated as components of the Martian regolith (e.g., Ming and Gooding, 1988; Basu et al., 1998; Berkley and Drake, 1981; Bish et al., 2003; Dickinson and Rosen, 2003; Tokano and Bish, 2005; Cannon et al., 2015). Geochemical modeling shows that zeolites on early Mars are likely to have formed under alkaline (pH $>$ 8) conditions with low water/rock ratios and surface temperatures below 150 °C (e.g., Semprich et al., 2019, Zolotov and Mironenko, 2016). Since the hydrochemistry and climate of early Mars remain a mystery, identifying and mapping zeolites on the surface of Mars can be used to reconstruct not only the paleoclimate and paleohydrochemistry, but also the geological evolution of Mars. Ehlmann et al. (2009) detected analcime in craters near Antoniadi basin, west of Nili Fossae, using Compact Reconnaissance Imaging Spectrometer for Mars (CRISM) orbital data. Carter et al. (2013) conducted a large-scale investigation of hydrous minerals on Mars using CRISM and OMEGA (Observatoire pour la Mineralogie, l'Eau, la Glace et l'Activite) orbital imaging spectrometer data. They categorized zeolites and sulfates into one class due to the difficulty of distinguishing them using orbital data, though

they typically form in very different environments. However, based on the shape of the 1.9 m absorption band, they infer that more than 80% of minerals assigned to that class are likely zeolites. Sun and Milliken (2015) conducted a survey to identify hydrous minerals in 633 crater central peaks using CRISM data and only identified zeolites in 4.5% of them. These studies emphasized the difficulty of identifying and distinguishing non-analcime zeolites from sulfates using Visible-near Infrared – Shortwave Infrared spectral data. Zeolites have also not yet been reported from in situ observations on Mars or in Martian meteorites.

Therefore, the identification and delineation of prospective areas for zeolites on the surface of Mars could serve as a guide for further searches for zeolites using detailed orbital spectral image analysis and future in situ observations. Predictive modeling for mineral exploration, a widely used statistical and probabilistic reasoning method in geosciences, can be used in this case. Predictive modeling for mineral exploration follows specific steps and starts by defining a conceptual model for the exploration target. To define a conceptual model for exploration targets for the mineral type of interest (zeolite in this case) requires knowledge of the possible geological and geochemical formation processes of the target mineral. This knowledge allows exploration criteria to be defined, followed by the selection of suitable geoscience spatial datasets to be used, the extraction and enhancement of evidential features in each dataset, selecting mapping method(s) for each evidential feature, selecting method(s) for creating predictive map(s) from each evidential feature, and then integrating the predictive maps to create a predictive model and/or to map the prospective areas for the target mineral (zeolites) (Carranza, 2011). The preferred predictive model for this study should 1) accommodate the multiclass and continuous geodata, and 2) be sufficiently robust to handle the "information fuzziness" inherent to remote observational data (Porwal et al., 2003; Zimmermann, 1991). The combination of the weights-of-evidence method and Fuzzy set theory can fulfill both criteria flexibly and consistently.

The weights-of-evidence method (WEM) is commonly applied for mineral exploration, landslide susceptibility analysis, and hazard modeling (e.g., Neuhäuser and Terhorst, 2007; Bonham-Carter et al., 1989; Bonham-Carter, 1994). It has also been used for habitat quality assessments (e.g., Romero-Calcerrada and Luque, 2006), and even mapping the potential habitat of underground mushrooms (Yang et al., 2012). To map the potential mineral deposits, the model uses the location of known mineral occurrences to identify the favorable geological and environmental factors that can help map the potential distribution of the desired mineral (Bonham-Carter et al., 1989). Fuzzy set theory is also used for predictive mineral potential mapping since it provides a mathematical framework for combining and analyzing quantitative and qualitative data independent of their characteristics or source (Luo and Dimitrakopoulos, 2003; Porwal et al., 2003; Moon, 1998). Cheng and Agterberg (1999) proposed a hybrid fuzzy WEM, in which subjective or objective definitions of a fuzzy membership function of evidence can be supplemented by a more objective WEM-calculated definition

of conditional probabilities. Due to our limited knowledge of the formation conditions (geological, mineralogical, physical, and hydrological) of zeolites on Mars, a data-driven (empirical) approach was used. Data-driven methods typically assume that a sufficient number of known zeolite occurrences within the study area have been well studied and documented (Porwal et al., 2003). Since there are no well-studied and documented zeolite detections on Mars, this study first models the favorable areas for hydrous minerals and based on that model identifies the favorable areas for zeolites using other information and assumptions.

The conceptual model developed in this study requires: 1) the suitable geologic and hydrologic environments for the formation of hydrous minerals, which are commonly formed under lacustrine, hydrothermal, diagenesis/metamorphic, or pedogenic processes, and 2) the presence of volcanic ash (tuff) as a starting material for the formation of zeolites. Therefore, as a first step, this study creates a predictive model (map) for the potential areas for hydrous minerals on Mars, and then based on the available information and models of distribution of pyroclastic ash deposits of Mars, create a predictive model (map) for the most likely areas for zeolites on the surface of Mars.

2 Datasets

2.1 Hydrous mineral Map

Hydrous minerals are important markers of the surface and subsurface conditions on early Mars since their crystal structures contain water and thus evidence of ancient water-related processes. Carter et al. (2013) conducted a global survey of Martian hydrous minerals using CRISM and OMEGA hyperspectral data and sorted their hydrous detections into nine classes of spectra: 1) Fe/Mg - phyllosilicates, 2) chlorites, 3) Al-smectites/micas, 4) Al-rich kaolins, 5) opaline silica, 6) zeolites/sulfates, 7) serpentines/carbonates, 8) prehnite, and 9) epidote. Based on their study, the most common Martian hydrous minerals are Fe/Mg- phyllosilicates (~89% of all hydrous exposures), followed by the Al-phyllosilicates (~33% of all hydrous exposures). Over 50% of global hydrous mineral detections by Carter et al. (2013) are associated with impact structures (e.g., central peaks, rims, walls, or ejecta). Around 20% are associated with horizontal/sub-horizontal sedimentary deposits, while alluvial fans/deltas are about 5% of the cases. Around 20% of the cases are associated with crustal outcrops. The database of detected hydrous mineral locations by Carter et al. (2013) was downloaded from https://www.cosmos.esa.int/web/psa/mars-maps.

2.2 Geology

The geologic map of Mars provides unique information on the spatial and temporal sequences of geological processes on the surface of Mars. Tanaka et al. (2014) applied photogeologic mapping techniques to map 44 geologic units and 13 linear feature types, categorizing units on the surface based on the timing of major episodes and the types of materials involved (Tanaka et al., 2014). The geological units are mapped using brightness, characteristics of the morphology

and topography, and relative ages based on impact crater densities and superposition. The geology map, created by Tanaka et al. (2014), was downloaded from https://pubs.usgs.gov/sim/3292/.

2.3 Elemental abundances

The abundance and distribution of elements on the Martian surface helps us understand how Mars formed and evolved (Boynton et al., 2007). In situ observations by landers and rovers provide more detailed mineralogic and elemental information for a few specific sites on the Martian surface, as has the analysis of Martian meteorites. The Gamma Ray Spectrometer (GRS) on the 2001 Mars Odyssey Mission (Boynton et al., 2004) detects gamma rays produced in rock and soil near the surface, providing some element data. The gamma rays measured are generated only within a few tens of centimeters of the surface and the measurements are complicated by differences in the size and composition of the rocks, different amounts of near-surface water, compositional variations with depth, and the atmosphere (Evans and Squyres, 1987). Poulet et al. (2007) mapped H, Si, Cl, K, and Th concentrations measured by the GRS for $\pm \sim 45°$ latitudes assuming that all elements are homogeneous in the top few tens of centimeters of surface materials. Detailed discussion of gamma-ray spectral data processing to determine elemental concentrations can be found in Boynton et al. (2004) and Poulet et al. (2007). For this study, two map products by Poulet et al. (2007), $2°\times 2°$ and $5°\times 5°$ binned point data, were downloaded from http://grs.lpl.arizona.edu/data.

2.4 Mineralogy

The concepts of mineral occurrences and associations are important to infer the identity of unidentified target minerals. Bandfield (2002) produced a global mineral distribution map using data from the Thermal Emission Spectrometer (TES) on the Mars Global Surveyor (MGS) spacecraft (Christensen et al., 1992). He used linear spectral deconvolution method to extract mineral abundance information and to remove atmospheric components form the TES data at a 1 pixel per degree (ppd) spatial resolution. He selected emissivity spectra of 32 minerals, glass, 6 atmospheric endmembers, and a blackbody spectrum to fit the 73 spectral channels of the TES data. The output was binned global mineral concentration maps (at a one pixel per degree resolution) including 1) sheet silicates and high-Si glass, 2) sulfate, 3) plagioclase, 4) hematite, 5) carbonate, 6) K-feldspar, 7) basaltic glass, 8) quartz, 9) High-Ca pyroxene, 10) low-Ca pyroxene, 11) olivine, 12) amphibole, and 13) RMS (root mean square error) maps. Mineral concentrations were calculated based on signal strength relative to the mineral endmembers used in the linear spectral deconvolution method.

Poulet et al. (2007) produced maps of the global distribution of Martian surface material based on the data from one Martian year of OMEGA observations. Global maps of hydrated minerals, mafic minerals, and ferric phases were derived using spectral parameters. Ody et al. (2012) produced maps detailing the global distribution of these mineral species using the entire OMEGA dataset

acquired from January 2004 to August 2010, when the 1 - 2.5 m channel cooler failed. Since the 1 - 2.5 m regions are important to discriminate most martian mineralogy, these global maps can be considered the final outcome of OMEGA observations (Ody et al., 2012). Mapping was done at a spatial resolution of 32 ppd (~ 2 km at the equator).

The global mineral abundance maps derived both from TES by Bandfield (2002) and from OMEGA by Ody et al. (2012) were download from https://www.cosmos.esa.int/web/psa/mars-maps.

2.5 Albedo

A NIR (Near Infrared) 1 m albedo (lambertian albedo) map produced by Ody et al. (2012) using the I/F/cos(i) value at 1.08 m (where i = solar incident angle) of OMEGA data from January 2004 to August 2010 was used for this study. The TES bolometric albedo global map with 8 ppd spatial resolution (Christensen et al., 2001) was also used. Observations of the surface albedo of Mars show significant changes over time, likely due to global dust storms that redistribute dust (Pleskot and Miner, 1981; Putzig and Mellon, 2007).

2.6 Thermal inertia

Thermal inertia (I) combines bulk thermal conductivity (k), density ( ), and heat capacity (c), as described by the formula I=√k c. Thermal inertia will generally be low for surfaces of fine-grained, unconsolidated materials, intermediate for cemented surfaces or those dominated by sand-sized grains, and high for rocky surfaces and bedrock outcrops (Putzig and Mellon, 2007). Therefore, the thermal inertia of a certain location on Mars is typically consistent with properties including the abundance of rocks, particle size, extent of bedrock exposure, degree of induration, and how these properties are combined within the field of view (Mellon et al., 2000). Putzig and Mellon (2007) have produced nighttime and daytime seasonal maps of apparent thermal inertia using three years of TES data at 1/20 ppd. They have cropped each of the 36 seasonal maps latitudinally and used the median values to create daytime and nighttime thermal inertia maps. These two maps were downloaded from https://www.mars.asu.edu/data/.

2.7 Dust cover

TES spectra provide information about apparent particle size effects, which can serve as a proxy for the presence of dust on the Martian surface (Ruff and Christensen, 2002). Ruff and Christensen (2002) introduced a dust cover index (DCI) defined by the average emissivity value in the wavelength region from 1350 to 1400 cm^{-1}. They have produced a DCI map using nadir-pointing, daytime TES spectral data with brightness temperature > 260 K. The TES were binned at 8 ppd, with any gaps filled using linear interpolation. This DCI map was downloaded from http://www.mars.asu.edu/~ruff/DCI/dci.html.

The dust index map derived from TES by Bandfield (2002) using the linear spectral deconvolution method was also used. The dust index maps show a remarkable spatial coherence with albedo and thermal inertia maps at many

scales. Dust free surfaces have very low albedo. However, thermal inertia is not well-suited for this due to its complex behavior for mixtures of dust and coarse particles (Ruff and Christensen, 2002).

2.8 Elevation and slope

The geology of terrestrial planets is mostly related to the morphology of the surface and therefore geological mapping also heavily relies on the morphology. Elevation information of the planetary surfaces is used to derive the morphology of the surface to analyze the landscape forms, processes, patterns, and evolution (Schumm, 1991). The elevation and slope maps were derived from the 463 m/pixel resolution of digital elevation data (DEM) from Mars Orbiter Laser Altimeter (MOLA) on Mars Global Surveyor (MGS) (Smith et al., 2001). The MOLA DEM data was downloaded from https://astrogeology.usgs.gov.

2.9 Valley networks

The study of fluvial systems observed on the surface of Mars is important for determining the aqueous history of Mars. Several global valley network maps on Mars have been produced both manually from Viking data (Carr and Chuang, 1997), MOLA and THEMIS data (Hynek et al., 2010), and THEMIS, CTX, and MOLA data (Alemanno et al., 2018), and automated mapping using MOLA data (Luo and Stepinski, 2009). The global valley network map produced by Alemanno et al. (2018) was used in this study. They used topographic data (MOLA) and photographic (THEMIS daytime IR and CTX) data to manually map all valleys with total lengths > 20 km. Mapping classes include 1) valley networks, 2) longitudinal valleys, 3) valleys on volcanoes, 4) valleys adjacent to canyons, 5) single valleys and valley segments, and 6) small outflow channels. The global geologic map of Mars, created by Tanaka et al. (2014), included three classes of valleys, 1) single valley, 2) small outflow valley, and 3) trough fluvial valley. These segment maps were used in this study.

2.10 Pyroclastic deposits

Explosive volcanic eruptions were likely frequent during the Noachian and Hesperian periods (Wilson and Head, 2007). The fine-grained pyroclastic deposits produced by explosive volcanism are difficult to identify via remote sensing techniques (Broz et al., 2020). The most commonly used method for identifying potential Martian pyroclastic deposits includes identifying 1) areas with high friability, 2) a small grain-size inferred from maps of low thermal inertia, 3) location near potential volcanic vents, 4) layering, 5) low albedo materials, 6) resurfaced areas near potential volcanic vent/constructs, and 7) mantle-like draping over topography (Broz et al., 2020 and references therein). Potential pyroclastic deposits identified previously based on these characteristics result in an area of $\sim$ 12.4 to 13.4 million km^2 ($\sim$ 8.6 - 9.3% of the martian surface) (Broz et al., 2020). This study uses a map of deposits identified in the literature as potentially pyroclastic that are larger than 10^5 km^2 (Broz et al., 2020; Tanaka, 2000; Kerber et al., 2012). The mapped deposits include Arabia deposits, Electris deposits, Medusae Fossae Formation, Dorsa Argentea Formation, Hellas

deposits, Argyre deposits, Tyrrhena Patera deposits, and Isidis deposits.

Kerber et al. (2013) simulated ancient Martian explosive eruptions (assuming a range of higher atmospheric pressures: 50 mbar, 0.5 bar, 1 bar, and 2 bar) using a planetary global circulation model developed by the Laboratoire de Meteorologie Dynamique (LMD). Most Martian explosive volcanic centers date to the Hesperian, which likely had higher atmospheric pressure than at present (e.g., Ramirez, 2017). The particle size used for their simulation was 35 m in radius representing small, far-field ash. For this study, a combined ash distribution pattern map created by Kerber et al. (2013) from all major Martian volcanic centers, assuming each erupted 1.4×10^6 km^3 of ash during their lifetimes under 1 bar of pressure, was selected.

2.11 Open and closed basins

The study of paleolakes on Mars is important because these can capture the record of geological and hydrological events within their catchments, and the seasonal and orbital cyclic changes through their sedimentary records (Cabrol and Grin, 2002). Possible paleolake basins observed on Mars have been cataloged and categorized into two main groups based on their morphological features: 1) Closed-basin lakes with an inlet valley and no outlet valley, and 2) Open-basin lakes having inlet valleys and outlet valleys (Cabrol and Grin, 1999; Fassett and Head, 2008; Goudge et al., 2015, 2012, 2016). For this study, the open and closed-basin lakes catalog compiled by Goudge et al. (2016) was used. The database consists of the locations of 205 closed-basin lakes (Goudge et al., 2015) and 220 open-basin lakes (Goudge et al., 2012; Fassett and Head, 2008). However, this database does not contain potential paleolakes without inlet valleys (like Columbus crater; Wray et al., 2011), even though this type of paleolakes may have been common on early Mars.

3 Methods

3.1 Preparation of factor maps

All the factor maps discussed above were imported into ILWIS via GDAL and ISIS3. The ILWIS (Integrated Land and Water Information System) is geographical information system (GIS) and remote sensing software developed by the Faculty of Geo-Information Science and Earth Observation (ITC) at the University of Twente, the Netherlands. Since 2007, ILWIS is freely available as an open-source software under the 52^o North initiative (https://www.itc.nl/ilwis/). GDAL (Geospatial Data Abstraction Library) is an open-source translator library for raster and vector geospatial data formats (https://gdal.org/). The ISIS3 (Integrated Software for Imagers and Spectrometers - version 3), developed and maintained by the U.S. Geological Survey, is an image processing software package capable of importing raw NASA planetary mission data into a usable geospatial image product (https://isis.astrogeology.usgs.gov/). All analysis was done using ILWIS (running on Linux Pop-OS), followed by reprojecting to a common coordinate system (Plate Carree projection system),

and resampling into 200 m/pixel resolution using the nearest neighbor method.

Total hydrous mineral locations detected by Carter et al. (2013) are shown in the Figure 1. The abundance of those hydrous mineral detections along with the latitudes are shown in the density plot in the Figure 1. This shows that more than 90% of the total detections (1735/1855) are in the area between latitudes 40^oN and 40^oS. The size of a 32-bit global factor map was around 45.5 GB, and most of the maps used in this study are 32-bit (the rest are 8-bit). Much memory space, computational power and computational time is required for map calculations. Each processing steps also produces intermediate maps mostly similar in size to the original map. Since the importance of the map classes/area are calculated based on the locations of hydrous mineral detections, the limited detections in the area beyond 40^oN and 40^oS latitudes will be less important. Therefore, to reduce the computational power, time, and memory space, sub maps were created from all the factor maps covering the area between latitudes 40^oN and 40^oS for the rest of the work.

FIGURE 1 HERE

Figure 1: Map of hydrous mineral detections on Mars. Each point represents the location of a hydrous mineral detection by CRISM and/or OMEGA. Background is a grayscale hillshade map created from MOLA DEM. Point density plot shows on the left side of the map.

All the continuous data raster maps (e.g., elevation, dust cover index, elemental abundance, etc.) were reclassified into ten classes after careful examination of the histograms of the pixel values and based on the discussions in the corresponding literature. The discontinuous data raster maps (categorical maps, e.g., geology map) were imported as is. The ten buffer regions (A: 0 - 200 m, B: 200 - 400 m, C: 400 - 600 m, D: 600 - 800 m, E: 800 - 1000 m, F: 1000 - 2500 m, G: 2500 - 5000 m, H: 5000 - 10000 m, I: 10000 - 100000 m, and J: $>$ 100000 m) were created from the segment maps and then rasterized. Based on the spatial association of buffer regions with the hydrous mineral detections, three buffer maps were selected. The boundaries of all the possible closed and open-basin lakes were manually digitized with the help of MOLA DEM. Two binary maps were created from the ash deposits map (ash deposit = 1, other area = 0) and open and closed paleolake basin map (open/closed basins = 1, other area = 0).

The total hydrous mineral detections within the sub map area (1735 points) were divided into two classes (train and test) using the stratified random sampling method. The H_2O weight percentages at each point location were extracted from the H_2O GRS map for the stratified random sampling method assuming that hydrous mineral abundances at each point location can be represented by the GRS H_2O map. Data partition was done using "caret" package in R. The train point map contains ~80% (1391 points) of the total points, while the test point map contains the rest of the data points (~20%, 344 points). The factor maps used in this study are listed in Table 1, and each factor map is referred to using the MapID in the rest of the text.

Table 1: Factor maps used in this study.

#	Platform	Product	MapID	Reference
	RASTER			
1	OMEGA	NIR albedo	om_albdo	Ody et al. (2012)
2		Fe^{3+}	om_fe530	
3		nphsFe^{3+}	om_nnphs	
4		Pyroxene	om_pyrox	
5		Olivine Spectral Parameter1	om_osp1m	
6		Olivine Spectral Parameter2	om_osp2m	
7		Olivine Spectral Parameter2	om_osp2m	
8	TES	Albedo	ts_albdo	
9		Amphibole	ts_amphi	Bandfield (2002)
10		Carbonate	ts_carbo	
11		High Calcium Pyroxene	ts_hcpmp	
12		Low Calcium Pyroxene	ts_lcpmp	
13		Hematite	ts_hemat	
14		K-feldspar	ts_kfeld	
15		Olivine	ts_olvne	
16		Plagioclase	ts_plgcl	
17		Quartz	ts_quatz	
18		Sulfate	ts_sulft	
19		Dust	ts_dustm	
20		Dust Cover Index (DCI)	ts_dcimp	Ruff and Christensen (2002)
21		Thermal Inertia-Day	ts_tiday	Putzig and Mellon (2007)
22		Thermal Inertia-Night	ts_tingt	
23	GRS	H_2O	gr_h2omp	Boynton et al. (2007)
24		Si	gr_simap	
25		K	gr_kmaps	
26		Cl	gr_clmap	
27		Fe	gr_femap	
28		Th	gr_thmap	
29	VIKING	Global Mosaic 232m v2	vk_color	USGS Astrogeology
30	MGS	MOLA DEM	mg_mldem	Smith et al. (2001)
31		Hilshade map from MOLA	mg_hilsd	
32		Slope map from MOLA	mg_slope	
	VECTOR			
33		Geology Map of Mars 2014	tn_geolo	Tanaka et al. (2014)
34		Hydrous mineral map	ct_hydst	Carter et al. (2013)
35		Open-closed basins	tg_basin	Goudge et al. (2016)
36		Valley Network	ga_vlnet	Alemanno et al. (2018)
37		Long Valley	ga_logvl	Alemanno et al. (2018)
38		Trough Fluvial	tn_trflu	Tanaka et al. (2014)
39		Pyroclastic ash distribution	lk_pyash	Kerber et al. (2013)
40		Pyroclastic deposits	pb_pydep	Broz et al. (2020)

3.2 Weights-of-evidence method (WEM)

The WEM was originally developed in the field of quantitative medical diagnosis and later used to the prediction of mineral deposits by Bonham-Carter et al. (1989). This empirical approach can calculate the relative importance of individual evidence maps using statistical methods (Bayesian relation) under the assumption that all variables are conditionally independent of mineral occurrences (Pan and Harris, 2000). For simplicity, the integration of two explanatory binary maps by WEM will be discussed. The two explanatory indicator maps, the pyroclastic ash deposits map and closed basins map as examples in this case, are denoted by A and C, respectively. The single target indicator variable, in this case the location map of detected hydrous minerals, is indicated by H. These maps are regarded as random variables that are either present or absent (binary) in a unit cell. The possible relations between C, A, and H are shown in Figure 2 Venn diagram. $\bar{A}$, $\bar{C}$, and $\bar{H}$ represent the absence status of A, C, and H, respectively.

FIGURE 2 HERE

Figure 2: Venn diagram for the relations between binary patterns.

The prior probability $P\{H\}$ is the probability of the occurrence of hydrous minerals in the entire study area, which can be calculated using the ratio of detected hydrous mineral pixels (or area), H to the total number of pixels in the study area (or total area), T.

$p(H) = \frac{H}{T}$ ———————— (eq. 1)

The relations between A, C, and H can be expressed by eight probabilities based on the assumption of conditional independence between A and C with respect to H.

$$p\left(\mathrm{ACH}\right), p\left(\mathrm{AC}\bar{H}\right), p\left(A\bar{C}H\right), p\left(\bar{A}\mathrm{CH}\right), p\left(\bar{A}\bar{C}H\right), p\left(\bar{A}C\bar{H}\right), p\left(A\bar{C}\bar{H}\right), p\left(\bar{A}\bar{C}\bar{H}\right)$$

These eight probabilities are mutually related by,

$p\left(\mathrm{ACH}\right) = p\left(A|H\right) p\left(C|H\right) p(H)$ ———————— (eg. 2)

$p\left(\mathrm{AC}\bar{H}\right) = p\left(A|\bar{H}\right) p\left(C|\bar{H}\right) p\left(\bar{H}\right)$ ———————— (eq. 3)

Based on the above relations, four conditional probabilities (posterior probabilities) can be calculated. As an example,

$p\frac{(A)}{(H)} = \frac{p(A)\times p(H/A)}{p(H)}$ ————————- (eq. 4)

where H is the occurrence of hydrous minerals, A is the pyroclastic deposits map, and $p(H/A)$ is the conditional probability of having hydrous minerals in the area where pyroclastic deposits are present.

Four weights, W_A^+, W_A^-, W_C^+, and W_C^-, can be calculated for each evidence class and these weights are dependent on the spatial relationship between the potential occurrence of hydrous minerals and the selected evidence map.

$W_A^+ = \ln\{p\left(A|H\right)/p\left(A|\bar{H}\right)\}$, $W_A^- = \ln\{p\left(\bar{A}|H\right)/p\left(\bar{A}|\bar{H}\right)\}$—— (eq. 5)

$W_C^+ = \ln\{p\left(C|H\right)/p\left(C|\bar{H}\right)\}$, $W_C^- = \ln\{p\left(\bar{C}|H\right)/p\left(\bar{C}|\bar{H}\right)\}$—— (eq. 6)

W^+ in each evidential map indicates the importance of the presence of the factor class for the occurrence of hydrous minerals. Positive W^+ values for a factor class indicate its favorability for the occurrence of hydrous minerals, while negative W^+ values denote unfavorability. W^- is used to evaluate the importance of the absence of a factor class for the occurrence of hydrous minerals. If W^- is positive, it indicates that the absence of the factor class creates the area more favorable for the occurrence of hydrous minerals. If W^- is negative, absence of the factor class is unfavorable. Zero weights do not show a correlation between the factor class and hydrous mineral occurrences.

The contrast ($C = W^+ - W^-$) represent the strength of association between the explanatory map (e.g., pyroclastic deposit map, A) and the target map (e.g., detected hydrous mineral location map, H). Large contrast values imply strong association between two factors while small contrast values indicate the opposite. The studentized contrast (C_{std}, also called the normalized contrast) is defined as the ratio of C to its standard deviation ($S(C)$) and is used as an indicator of confidence.

$C_{\text{std}} = \frac{C}{\sqrt{S^2(W^+)+S^2(W^-)}}$ ———————— (eq. 7)

where, $S^2\left(W^+\right)$ and $S^2\left(W^-\right)$ are the variances of W^+ and W^-, respectively.

The hydrous mineral train points (1391 points) were used to calculate the weight values (W^+, W^-), C, and C_{std} for each class in each map. Based on the weights and C_{std}, the study proceeded with the 30 selected factor maps (Table 2). These maps are spatially highly correlated (positively and negatively) with the hydrous mineral detections.

3.3 Fuzzy Set Theory

Most tools used for formal reasoning, modeling, and computing are deterministic, precise, and crisp. They are yes-or-no-types rather than more-or-less types. As an example, zeolite is present-or-not in a closed basin of Mars, instead of more possibility/ less possibility (can be/ cannot be) present. In classical set theory, an element either belongs to a set or not, the same as in optimization, and a solution is therefore either feasible or not. Fuzzy set theory, coined by Lotif A. Zadeh (Zadeh, 1965), involves capturing, exemplifying, and working with linguistic notions-objects for which boundaries are unclear. While the Boolean set theory defines a membership value of either 1 or 0 (true or false), the fuzzy set theory defines the degree of membership in a set, represented by values between 0 and 1.

Let X be a collection of objects, with a generic element of X denoted by x.

Thus, X = $\{x\}$.

A fuzzy set A in X is characterized by a membership function (or grade of membership or degree of compatibility or degree of truth) $f_A(x)$ which associates with each object in X a real number in the interval [0,1], with the value of $f_A(x)$ at x representing the grade of membership of x in A. The membership function of a fuzzy set A is denoted by μ_A and its form is

$\mu_A : X \rightarrow [0,1]$ ——————— (eq. 8)

Typically, a fuzzy model consists of the following feedforward modules, 1) a fuzzifier (encoder: converts input categorical or numerical data into fuzzy values), 2) an inference engine (processor: the mind of the fuzzy model, simulates the human decision-making process), and 3) a defuzzifier (decoder: converts a synthesized fuzzy set back to a crisp set using a mathematical function or a subjectively or objectively defined threshold fuzzy value).

3.3.1 Fuzzifier: Fuzzification of Predictor Maps The value of the membership function can be calculated using two methods; 1) calculate the membership function using a membership function curve, 2) assign membership values for each class artificially based on expert knowledge of the system concerned. In this study both methods were adopted. For the factor maps of valley network (ga_vlnet), ash thickness (lk_pyash), and map of open/closed basins (tg_basin), fuzzy membership values were added manually, while the fuzzy membership values for the rest of the maps were calculated using membership function curves.

In this study, four membership functions were modeled, and results were compared to select the best method. The methods include membership function calculation using positive weight (W^+), contrast (C), and studentized contrast (C_{std}) of each map unit calculated using the WEM method.

3.3.1.1 **Method 1 (Zimmermann, 1991).** Logistic membership function, $\mu_A(x)$,

$\mu_A(x) = \frac{1}{1+e^{-a(w_{\text{pij}}-b)}}$ ——————— (eq. 9)

where, w_{pij} is the positive weight of the j^{th} class of the i^{th} evidential map (fuzzy set), b is a specified fuzzy score at cross-over point for the function, and a is a specified slope of the function at cross-over point. Slope values, a, used for each factor map are shown in table 2. The value of the cross-over point, b, is assigned as 0.5. The logistic membership function transforms the class weights into fuzzy membership values range from 0 to 1.

3.3.1.2 **Method 2 (Cheng and Agterberg, 1999).** Fuzzy membership values were calculated using the contrast values in each evidential map,

$\mu_A(x) = \frac{C_{\text{ij}}-C_{\text{min}}}{C_{\text{max}}-C_{\text{min}}}$ ——————— (eq. 10)

where, $C_{\max}$ and $C_{\min}$ are the maximum contrast ($C_{\max} = \max(W^+ - W^-)$), and the minimum contrast of the i^{th} fuzzy set, respectively. C_{ij} is the contrast value of the j^{th} class in the i^{th} evidential map.

3.3.1.3 **Method 3 (Porwal et al., 2003).** Porwal et al. (2003) defined the piece-wise linear membership function as the fuzzifier in their model based on the contrast value. The membership value, $\mu_A(x_{\text{ij}})$ is calculated using

$$\mu_A(x) = \begin{cases} 0.01 & \text{if} \quad C_{\text{ij}} = C_{\min} \& C_{\min} < 0 \\ 0.5 - \frac{C_{\text{ij}}}{2 \times C_{\min}} & \text{if} \quad C_{\min} < C_{\text{ij}} \leq 0 \\ 0.5 + \frac{C_{\text{ij}}}{2 \times C_{\max}} & \text{if} \quad 0 \leq C_{\text{ij}} \leq C_{\max} \end{cases} \quad \text{——— (eq. 11)}$$

where, C_{ij} is the contrast value of the j^{th} class of i^{th} evidential map, and $C_{\min}$ and $C_{\max}$ are the minimum and maximum contrast values of the i^{th} map.

3.3.1.4 **Method 4 (this study)** This study employs a Logistic membership function, $\mu_A(x)$,

$$\mu_A(x) = \frac{1}{1+e^{-a((w_{\text{pij}} \times F)-b)}} \quad \text{———— (eq. 12)}$$

where w_{pij} is the positive weight of the the j^{th} class of i^{th} evidential map. b is a specified fuzzy score at the cross-over point for the function, a is a specified slope of the function at the cross-over point. Multiplication factor F was calculated using studentized contrast (C_{std}) of each class in each evidential map.

$$F = \begin{cases} 0.1 & C_{\text{std}} < 1.5 \\ 1.0 & C_{\text{std}} \geq 1.5 \end{cases} \quad \text{———- (eq. 13)}$$

The fuzzy membership values must show not only the relative importance of each map, but also the relative importance of each class (map units) in each map. Therefore, different slope values "a" were chosen for each map based on the importance of each map and their classes (map units) (Table. 2). The fuzzy membership function maps are named using the respective MapID followed by prefix fzm_.

Table 2: Slope "a" values used in Logistic membership functions (eq. 9 and 12).

Map 1 - 10	**a**	**Map 11 - 20**	**a**	**Map 21 - 30**	**a**
fzm_gr_femap	1	fzm_ts_kfeld	1	fzm_gr_h2omp	3
fzm_gr_kmaps	1	fzm_ts_olvne	1	fzm_om_fe530	4
fzm_om_osp1m	1	fzm_ts_plgcl	1	fzm_om_nnphs	4
fzm_om_osp2m	1	fzm_ts_sulft	1	fzm_tn_geomp	5
fzm_om_osp3m	1	fzm_gr_simap	2	fzm_gr_clmap	5
fzm_om_pyrox	1	fzm_gr_thmap	2	fzm_mg_mldem	5
fzm_ts_amphi	1	fzm_ts_carbo	2	fzm_om_albdo	5
fzm_ts_hcpmp	1	fzm_ts_quatz	2	fzm_ts_albdo	5
fzm_ts_lcpmp	1	fzm_ts_tiday	2	fzm_ts_dcimp	5

Map 1 - 10	**a**	**Map 11 - 20**	**a**	**Map 21 - 30**	**a**
fzm_ts_hemat	1	fzm_ts_tingt	2	fzm_ts_dustm	5

The fuzzy membership values of the different map units in the geologic map calculated using the above four methods are shown in Figure 3. This shows that the method developed in this study (Method 4) performs the best and was therefore chosen as the fuzzy membership calculation method for this study.

FIGURE 3 HERE

Figure 3: Calculation of fuzzy membership functions using different methods. The geology map (tn_geomp) was used as the example in this figure. The Weight W^+ x-axis refers to Method 1 (Zimmermann, 1991) and Method 4 developed in this study, while the Contrast C x-axis refers to Method 2 (Cheng and Agterberg, 1999) and Method 3 (Porwal et al., 2003).

Figure 4 plots the fuzzy membership values against the geological map units in (relative) chronological order. It shows that high fuzzy membership values were received for the Noachian age terrains, where most hydrous mineral detections were found (Carter et al., 2013). Hesperian and Noachian highland undivided (HNhu) and Hesperian transition terrains (Htu and Ht) show high Fuzzy membership values after high values seen in Early and Middle Noachian highland massifs (mHnm and eNhm). The peak observed at the Late Noachian to Early-Hesperian transition has been proposed as an epoch of intense surface flow (Irwin et al., 2005). Carter et al. (2013) observed fewer hydrous mineral exposures in Hesperian aged terrain, and a negligible number of hydrous mineral exposures in Amazonian-aged terrains. Figure 4 also shows a peak for Amazonian and Hesperian impact (AHi). This might be due to the delivery of preexisting clay-rich material underneath more recent terrains to the surface by impact excavation (Barnhart and Nimmo, 2011). It is also important to note that the number of hydrous mineral occurrences corresponding to a geologic units does not necessarily reflect the time of their formation. Those hydrous mineral detections can be younger (e.g., weathering) or older (e.g., transported from other places and deposited) than the outcrop (geologic unit) in which they are present (Carter et al., 2013).

FIGURE 4 HERE

Figure 4: Calculated fuzzy membership values as a function of time (geological units). eNh: Early Noachian highland, eNhm: Early Noachian highland massif, mNh: Middle Noachian highland, mNhm: Middle Noachian highland massif, Nve: Noachian volcanic edifice, Nhe: Noachian highland edifice, Nhu: Noachian highland undivided, lNH: Late Noachian highland, lNv: Late Noachian volcanic, HNb: Hesperian and Noachian basin, ANa: Amazonian and Noachian apron, HNt: Hesperian and Noachian transition, HNhu: Hesperian and Noachian highland undivided, Htu: Hesperian transition undivided, Ht: Hesperian transition,

eHh: Early Hesperian highland, eHb: Early Hesperian basin, eHv: Early Hesperian volcanic, eHt: Early Hesperian transition, Hve: Hesperian volcanic edifice, Hto: Hesperian transition outflow, lHv: Late Hesperian volcanic, lHb: Late Hesperian basin, lHl: Late Hesperian lowland, lHvf: Late Hesperian volcanic field, lHt: Lte Hesperian transition, AHtu: Amazonian and Hesperian transition undivided, AHv: Amazonian and Hesperian volcanic, AHi: Amazonian and Hesperian impact, eAb: Early Amazonian basin, mAl: Middle Amazonian lowland, Aa: Amazonian apron, Av: Amazonian volcanic, Ave: Amazonian volcanic edifice, lAa: Late Amazonian apron, lAv: Late Amazonian volcanic, lAvf: Late Amazonian volcanic field.

Fuzzy membership function values were manually added to the factor maps of valley network (ga_vlnet) and ash thickness (lk_pyash) (Table 3). These membership values were chosen arbitrarily based on subjective judgment about the relative importance of each class (map unit) in each factor map.

Table 3: Fuzzy membership values (fzm) in map classes of maps of valley networks (ga_vlnet) and ash thickness map (lk_pyash).

ga_vlnet distance class	**fzm_ga_vlnet**	**lk_pyash thickness class**	**fzm_lk_pyash**
0 - 200 m	1.0	0.00 - 6.25 m	0.1
200 - 400 m	0.9	6.25 - 12.50 m	0.2
400 - 600 m	0.8	12.50 - 25.00 m	0.4
600 - 800 m	0.7	25.00 - 50.00 m	0.5
800 - 1000 m	0.6	50.00 - 100.00 m	0.6
1000 - 2500 m	0.5	100.00 - 200.00 m	0.7
2500 - 5000 m	0.4	200.00 - 400.00 m	0.8
5000 - 10000 m	0.3	400.00 - 800.00 m	1.0
10000 - 100000 m	0.2		
> 100000 m	0.1		

Figure 5 shows the entire fuzzification process using MOLA DEM as an example. It shows the original MOLA DEM (a), classified MOLA DEM (b) and after assigning the calculated fuzzy membership values for each elevation class (c).

FIGURE 5 HERE

Figure 5: Fuzzification process showing the original MOLA DEM (a), classified MOLA DEM (b), and a map after assigning the fuzzy membership values for each elevation class (c).

3.3.2 Inference Engine The mind of a fuzzy model, the inference engine, uses the individual fuzzy sets conveyed by the fuzzifier while filtering out the informational noise to create a synthesized fuzzy set. A fuzzy inference engine consists of multiple serial or parallel networks that use fuzzy operators to sequentially combine fuzzy sets (Porwal et al., 2003). The most basic fuzzy operators

are fuzzy OR, fuzzy AND, fuzzy algebraic products, fuzzy algebraic sum, and fuzzy Gamma (γ) operator.

***3.3.2.1* Fuzzy OR** Fuzzy OR is similar to a Boolean OR (logical union), and the output membership values are controlled by the maximum values from any of the input maps, for any location. The fuzzy OR is defined as,

$\mu_X = \text{MAX}\,(\mu_A, \mu_B, \mu_C, ...)$ ———(eq. 14)

using this operator, the combined membership value at a specific location is represented by the most suitable evidence maps. As an example, several attempts were made to derive the abundance of olivine using OMEGA and TES data. This study selected four olivine maps as factor maps and used a fuzzy OR operator to integrate those maps to extract the most suitable locations for olivine. The fuzzy OR operator was used to create the maps listed below,

max_gr_clfek = MAX(fzm_gr_clmap,fzm_gr_femap,fzm_gr_kmaps)–(eq. 15)

max_olivine = MAX(MAX(fzm_om_osp1m,fzm_om_osp2,fzm_om_osp3), zm_ts_olvne)–(eq. 16)

max_pyrox = MAX(fzm_ts_lpcmp,fzm_ts_hcpmp,fzm_om_pyrox)–(eq. 17)

max_qtz_crb_hem = MAX(fzm_ts_quatz,fzm_ts_carbo,fzm_ts_hemat)–(eq. 18)

***3.3.2.2* Fuzzy AND** Fuzzy AND is similar to a Boolean AND (logical intersection) operation on classical set values of (0,1). It is defined as

$\mu_X = \text{MIN}\,(\mu_A, \mu_B, \mu_C, ...)$ ——————(eq. 19)

where, $\mu_A m, \mu_B, \mu_C, ...$ are membership values at a particular location (x, y) on map A, map B, map C, .., respectively. The effect of Fuzzy AND is to make it so the output map is controlled by the smallest fuzzy membership value at each location (Bonham-Carter, 1994). This rule is suitable for the places where two or more pieces of evidence must be present together for the hypothesis to be true. In this study, as an example, selecting the minimum albedo fuzzy membership value in each corresponding pixel in albedo fuzzy membership maps derived from both OMEGA and TES data will increase the confidence of the final albedo fuzzy membership map. The fuzzy AND operator was used to create the maps listed below,

min_dust_nnphs = MIN(fzm_ts_dustm,fzm_ts_dcimp,fzm_om_nnphs)–(eq. 20)

min_om_ts_albdo = MIN(fzm_om_albdo,fzm_ts_albdo)–(eq. 21)

min_ti_day_ngt = MIN(fzm_ts_tiday,fzm_ts_tingt)–(eq. 22)

min_gr_clfek = MIN(fzm_gr_clmap,fzm_gr_femap,fzm_gr_kmaps)–(eq. 23)

Finally, six maps were created combining the above fuzzy membership maps.

min_physical = MIN(min_dust_nnphs,min_om_ts_albdo,min_ti_day_ngt)–(eq. 24)

max_physical = MAX(min_dust_nnphs,min_om_ts_albdo,min_ti_day_ngt)–(eq. 25)

min_elements = MIN(min_gr_clfek,fzm_gr_simap,fzm_gr_h2omp)–(eq. 26)

max_elements = MAX(max_gr_clfek,fzm_gr_simap,fzm_gr_h2omp)–(eq. 27)

min_minerals = MIN(max_olivine,max_pyrox,max_qtz_crb_hem)–(eq. 28)

max_minerals = MAX(max_olivine,max_pyrox,max_qtz_crb_hem)–(eq. 29)

Figure 6 shows two output maps created from two different set of fuzzy operators. Though the input maps for both sets were the same, different output maps were made based on the fuzzy operators used (eq. 24 and 25).

FIGURE 6 HERE

Figure 6: Integrated fuzzy membership maps. a) Max_physical (eq. 25), and b) Min_physical (eq. 24).

***3.3.2.3* Fuzzy Algebraic Product (FAP)** The combined membership function is defined as

$\mu_X = \prod_{i=1}^{n} \mu_i$ ——————(eq. 30)

where μ_i is the fuzzy membership function for the i-th map and i = 1, 2, 3, ..., n maps are to be combined. The combined fuzzy membership values tend to be very small with this operator, due to the effect of multiplying several numbers less than 1. The output is always smaller than, or equal to, the smallest contributing membership value, and is therefore "decreasive."

***3.3.2.4* Fuzzy Algebraic Sum (FAS)** Fuzzy algebraic sum is complementary to the fuzzy algebraic product and defined as

$\mu_X = 1 - \prod_{i=1}^{n} (1 - \mu_i)$ ——————(eq. 31)

The result is always larger or equal to the largest contributing fuzzy membership value. The effect is therefore "increasive." The pieces of evidence that both favor a hypothesis reinforce one another and the combined evidence is more supportive than either piece of evidence taken individually. It is also important to note that whereas the fuzzy algebraic product is an algebraic product, the fuzzy algebraic sum is not an algebraic summation (Bonham-Carter, 1994).

Six map combinations were selected using seven input maps created during the previous step (Table 4). From these 6 map combinations, twelve maps were created calculating fuzzy algebraic product (FAP) and fuzzy algebraic sum

(FAS). The resulting fuzzy algebraic products (FAP) and algebraic sum (FAS) maps for the sixth map combination (FAP_6 and FAS_6 in Table 4) are shown in Figure 7.

Table 4: Input map combinations used to create 12 map combinations. FAP: fuzzy algebraic product. FAS: fuzzy algebraic sum.

Map combination	**FAP_1 FAS_1**	**FAP_2 FAS_2**	**FAP_3 FAS_3**	**FAP_4 FAS_4**	**FAP_**
min_physical	x		x	x	
max_physical		x			x
min_elements			x		
max_elements	x	x			
min_minerals	x		x		x
max_minerals		x		x	
fzm_geology	x	x	x	x	x

FIGURE 7 HERE

Figure 7: Fuzzy algebraic product (FAP) and fuzzy algebraic sum (FAS) maps of map combination 6 (FAP_6$andFAS$_6) listed in Table 4.

***3.3.2.5* Gamma (γ) operation.** Gamma operation is defined in terms of fuzzy algebraic product and the fuzzy algebraic sum by

$$\mu_X = (\text{Fuzzyalgebraicsum})^{\gamma} * (\text{Fuzzyalgebraicproduct})^{1-\gamma} \text{————(eq. 32)}$$

where γ is a parameter chosen in the range of 0 to 1 (Zimmermann and Zysno, 1980). When is 0, the combination equals the fuzzy algebraic product, and when the γ is 1, the combination is equals the fuzzy algebraic sum. A wise selection of γ creates output values that ensure a flexible compromise between the "increasive" effects of the fuzzy algebraic sum and the "decreasive" effects of the fuzzy algebraic product. The effect of choosing different values of gamma (γ) for combining two fuzzy memberships values is shown in Figure 8.

FIGURE 8 HERE

Figure 8: A graph of fuzzy membership obtained by combining two fuzzy membership values versus gamma.

Twenty-five (25) maps were calculated using different map combinations listed in Table 4 with different gamma values (Table 5). In other words, 25 inference network models were created. After visual and statistical analysis of all 25 maps, map combinations 2 (Fz_02) and 6 (Fz_06) in the Table 4 were selected for further analysis. Figure 9 shows the favorability coverage and the test and train accuracy of each map combination with respect to the gamma values. Favorability coverage was calculated based on the area higher than 0.5 fuzzy membership values (pixel values) compared to the total map area. This

shows that the percentage of (favorability) coverage and test and train accuracy of both map combinations increases with the increase of gamma values. The best predictive model in this case would be the model with the highest train and test accuracy with lowest spatial coverage. The test and train accuracy (success rate) higher than 80% were defined as the selection criteria and based on that a 0.84 gamma value was selected. However, both map combinations (F2 and F6) scored more than 80% accuracy, though the F6 shows higher spatial coverage than F2. Four favorability map classes were created from each map (Fz_02_0.84 and Fz_06_0.84) based on the favorability index (pixel values). Classes include Unfavorable (pixel value 0 - 0.25), Less favorable (pixel value 0.25 - 0.50), Favorable (pixel value 0.50 - 0.75), and Most favorable (pixel value 0.75 - 1.00). This step is called as defuzzification. Results were validated using train and test data sets. Table 6 shows the results of the accuracy assessment. The values are in percentages representing the number of data points in each class with respect to the total number of points in the dataset. This shows that Fz_06_0.84 (final map created using map combination F6 with 0.84 gamma value) shows the highest test and train accuracy for the most favorable class. Therefore, map F_06_0.84 was selected as the final map to depict the highest potential areas for hydrous minerals (Figure 10) and to identify the potential locations for zeolite in the next step.

Table 5: List of calculated 25 maps using different map combination and gamma values.

Map 1 - 5	**Map 6 - 10**	**Map 11 - 15**	**Map 16 - 20**	**Map 21 - 25**
Fz_01_0.65	Fz_02_0.80	Fz_02_0.85	Fz_03_0.97	Fz_06_0.82
Fz_01_0.75	Fz_02_0.81	Fz_03_0.85	Fz_04_0.85	Fz_06_0.83
Fz_01_0.85	Fz_02_0.82	Fz_03_0.90	Fz_05_0.85	Fz_06_0.84
Fz_01_0.90	Fz_02_0.83	Fz_03_0.95	Fz_06_0.80	Fz_06_0.85
Fz_01_0.95	Fz_02_0.84	Fz_03_0.96	Fz_06_0.81	Fz_06_0.86

FIGURE 9 HERE

Figure 9: Percentage of accuracy and spatial coverage in each map combination (F2 and F6) against different gamma values.

Table 6: Test and train accuracy (success rate) of each map combinations. This shows the number of hydrous mineral detections in each class as a percentage with respect to the total number of data points. The train dataset is indicated by letters "_trn" after the fuzzy map Fz_02_0.84 or Fz_06_0.84, while the test dataset indicated by letters "_tst".

Class	**Fz_02_0.84_trn**	**Fz_02_0.84_tst**	**Fz_06_0.84_trn**	**Fz_06_0.84_tst**
Unfavorable	0.1	0	0.3	0
Less favorable	18.9	16.5	13.1	10.4

Class	Fz__02__0.84__trn	Fz__02__0.84__tst	Fz__06__0.84__trn	Fz__06__0.84__tst
Favorable	75.5	78.5	54.6	57.3
Most favorable	5.5	5.0	32.0	32.3

FIGURE 10 HERE

Figure 10: a) Favorability map for hydrous minerals (Map Fz_06_0.84). The areas are ranked based on their fuzzy membership values. Fuzzy membership ranges from 0 to 1 (less favorable to highly favorable). b) Favorability class map derived from map (a) showing the potential area for the hydrous minerals on Mars up to 40 degrees latitude.

As discussed in the introduction, the greatest abundances of zeolites on Earth are found in volcaniclastic deposits. Therefore, it is hypothesized that zeolites are most likely to be found in places where pyroclastic deposits were subjected to aqueous alteration. The possible aqueous alteration areas were mapped using hydrous mineral detections in previous steps. Ash distribution patterns on Mars modeled by Kerber et al. (2013) were used to identify the most favorable areas for zeolites on early Mars. Ash thickness in their model is proportional to the possibility that zeolites could form, because great thickness can reflect a large amount of ash in the area or a high possibility of finding ash in the area according to the model. The map of possible pyroclastic deposits larger than $10^5 km^2$ is also used in this study to achieve more robust results. The open and closed basin paleolakes maps are finally used to select the most likely paleolake basins to look in for zeolites using detailed orbital studies. The ash thickness map modelled by Kerber et al. (2013), potential pyroclastic deposits (black outlines), and closed and open basin paleolakes (black filled areas) are shown in Figure 11. Ash thickness in the map is represented by the fuzzy membership values. Assigned fuzzy membership values positively increase with the modeled ash thickness (Table 3).

FIGURE 11 HERE

Figure 11: The map shows the thickness of possible ash deposits modelled by Kerber et al. (2013), pyroclastic ash deposits (black outline) compiled by Broz et al. (2020) and open and closed basins (black filled areas) compiled by Goudge et al. (2016). Values in the legend are fuzzy membership values corresponding to the thickness of the modeled ash deposits.

Figure 12 shows the three-stage inference engine used to create the final map. Only the inference engine (workflow) of the selected final map (Fz_06_0.84) was outlined here to make the flow chart clear and simple. At the first stage, all the fuzzified evidential maps which were created using the membership functions defined by the weight-of-evidence method were combined using fuzzy operators to result three intermediate fuzzy evidential maps (max_physical, max_mineral, tn_geolo). These maps were later combined using the fuzzy gamma (γ) operator to create the synthesized fuzzy favorability map for the hydrous minerals

(fav_hydrous). In the third step, hydrous mineral favorability fuzzy membership map was combined with ash thickness (lk_pyash), pyroclastic deposits (pb_pydep), and open and closed basin (tg_basin) maps to generate a favorability map for the zeolites.

FIGURE 12 HERE

Figure 12: The fuzzy inference engine used to crate map Fz_06.

4 Results and discussion

The potential zeolite bearing terrain map calculated using the data-driven fuzzy weights-of-evidence method is shown in Figure 13. This shows that the eastern and western Arabia deposits and some sites of Medusae Fossae Formation show the highest probability for finding zeolites within the previously mapped potential pyroclastic deposits. Areas of interest outside the mapped pyroclastic deposits include certain areas of Valles Marineris, Mawrth Vallis, highlands north of Hellas, and the Terra Cimmeria and Terra Sirenum regions. Since there is no ground truth yet to validate the resultant potential zeolite bearing map, the zeolite detection using orbital images and the geological and hydrological settings favorable for the formation of zeolites in the area based on the literature will be discussed. Favorable geological and hydrological settings for the formation of zeolites include tuff (volcanic ash deposits), water, and the presence of key hydrous minerals inferring near-surface temperature alteration, low-grade metamorphic alteration, or hydrothermal alteration.

FIGURE 13 HERE

Figure 13: Potential zeolite bearing terrains calculated using the data driven fuzzy weights-of-evidence method. Value range indicates the possibility of finding zeolite based on the calculations. 1 = highest possibility, 0 = Lowest possibility. Background is a hillshade from MOLA DEM.

4.1 Arabia Terra

Arabia Terra is a cratered Noachian highland area and is probably composed of a mixture of impact breccias and volcanic, aeolian, and fluvial deposits (Davis et al., 2019; Tanaka, 2000). The zeolite mineral analcime was first detected in the west of Nili Fossae in craters near the Antoniadi basin and in the eastern portion of the Arabia Terra by Ehlmann et al. (2009) using CRISM data. Ash dispersion modeling (e.g., Kerber et al., 2012; Kerber et al., 2013) suggests that extensive ash deposits should be common in the Arabia Terra. Fassett and Head (2007) observed the hundreds of meters of material deposited on the surface of the northeast Arabia Terra, likely as airfall. The fluvial systems in the region are interpreted to have been formed by precipitation and runoff during the mid-Noachian and early-Hesperian (Davis et al., 2016, 2019). Whelley et al. (2021) also identified the presence, thickness, and distribution of altered volcanic ash layers in Arabia Terra using orbital spectral data. They identified the interlayered sequence of volcanic ash units containing hydroxy sulfates, Fe/Mg-smectites, Al-smectites, aluminosilicates, and hydrated silica.

4.2 Medusae Fossae Formation

The Medusae Fossae Formation (MFF) in southern Elysium and northern Memnonia and Amazonis Planitia and Aeolis Planitia (Kerber and Head, 2010) is characterized by large accumulations of friable, fine-grained deposits most likely composed of volcanic ash, ignimbrites, or aeolian dust (Mandt et al., 2008; Kerber and Head, 2010). Both the Tharsis Montes and Elysium Montes could be the source of pyroclastic deposits. Modified and inverted fluvial channels indicate that there was some fluvial activity during the formation or modification of the MFF (Kerber and Head, 2010).

4.3 Valles Marineris

Viviano-Beck et al. (2017) compositionally mapped the Valles Marineris wall units and identified zeolites along with chlorite and carbonate on the north and south walls of eastern Coprates Chasma. They were spatially associated with olivine-rich dikes, suggesting hydrothermal alteration from primary igneous phases to zeolite (Viviano-Beck et al., 2017). The coexistence of zeolites and carbonates implies that the fluids were alkaline. A wide variety of hydrated mineral assemblages is also identified in a depression close to Noctis Labyrinthus, at the western end of Valles Marineris, where Fig 13 shows high probability of finding zeolites (e.g., Thollot et al., 2012). Mitrofanov et al. (2022) recently observed unusually high hydrogen abundances at Candor Chaos in the central area of Valles Marineris using the FREND (Fine Resolution Epithermal Neutron Detector) neutron telescope onboard ExoMars Trace Gas Orbiter (TGO). Based on these results, they concluded that the high (40.3%) mean derived Water Equivalent Hydrogen (WEH) value at the Candor Chaos could be related to locally large abundances of highly hydrated minerals or water ice permafrost.

4.4 Mawrth Vallis

Mawrth Vallis sits at the boundary between the northern lowlands and the southern highlands (Bishop et al., 2013) and hosts the largest outcrop of Al/Si-rich clays on Mars (Bishop and Rampe, 2016). The Al/Si-rich clay unit mainly consists of montmorillonite, opal, kaolinite/halloysite, aluminosilicates, and zeolite (Bishop et al., 2013). Bishop and Rampe (2016) have identified the poorly crystalline aluminosilicates as allophane and imogolite using CRISM and TES data. They suggested that the ash from one or many of the supervolcanoes identified in northern Arabia Terra could be the source of allophane + imogolite unit at Mawrth Vallis. Loizeau et al. (2012) estimated the age and duration of aqueous activity in the Mawrth Vallis region using crater counting. Michalski et al. (2013) developed multiple working hypotheses as to how the compositional stratigraphy at Mawrth Vallis region formed and their favored hypothesis for the observed compositional stratigraphy was that volcanogenic acidic aerosols and snow or ice and small volumes of water chemically altered tephra deposits.

4.5 North Hellas Highlands

The model also shows a high favorability for zeolites in the North Hellas highland

region. Terby crater in the North Hellas highlands hosts the thickest lake sediments yet observed on Mars (Ansan et al., 2011). Hargitai et al. (2018) mapped potential paleolakes to the northeast of Hellas Basin in the Navua-Hadriacus-Ausonia region, identifying 34 potentially paleolake-hosting depressions. These lakes may have formed in the Hesperian during a volcanically active period (Hargitai et al., 2018). Zhao et al. (2020) identified 64 paleolakes with diameters larger than 4 km. They observed lacustrine deposits, volcanic ash, aeolian sand deposits, exposures of bedrock, and impact breccia/melts in the area. Previous studies of the northwestern Hellas region showed high concentrations of aqueous minerals including carbonates, chlorides, sulfates, and phyllosilicates (Osterloo et al., 2010; Carter et al., 2013; Ehlmann and Edwards, 2014; Wray et al., 2016; Zhao et al., 2020).

4.6 Terra Cimmeria/Terra Sirenum Region

The Terra Cimmeria/Terra Sirenum region has light-toned knobs that contain phyllosilicates possibly formed by aqueous alteration of the fine-grained (potentially ashfall) Electris Deposit described by Grant and Schultz (1990). The clays in these deposits likely formed in a network of local lakes (Wendt et al., 2013). The mineralogical, morphological, and stratigraphical study of Terra Cimmeria/Terra Sirenum region done by Wendt et al. (2013) shows the long-lasting, complex aqueous history involving localized lakes, valley networks, and multiple stages of mineral alteration.

Missing data or misinterpreted patterns are two major sources of uncertainty in mapping mineral favorability. This is more critical in poorly explored areas where fewer data are available than in well-explored areas. Most areas on Mars are poorly explored. The fuzzy weights-of-evidence method adopted here provides a framework for calibrating fuzzy membership functions to replace missing data for posterior probability calculations (Cheng and Agterberg, 1999). Since the weights-of-evidence method is objective, it also avoids the subjective choice of weighting factors. The objective methods are more important in poorly explored areas where little knowledge is available. One of the main disadvantages of the weights-of-evidence method is that it is only applicable in regions where the response variable is fairly well known. If the response variable is poorly known for a certain region, the results must be interpreted with caution. The response variable used in this study is the location of hydrous minerals. Carter et al. (2013) discussed several biases and limitations for hydrous mineral detections, which can directly influence the probabilistic model applied here.

1. Carter et al. (2013) demonstrated that the detection capabilities of hydrous minerals on Mars using orbital data are limited by the pixel resolution of the instrument. Areas with hydrous minerals larger than the smallest ground resolution cell (~20m in CRISM) can be detected. In addition, orbital spectral data both from CRISM and OMEGA exhibit instrumental artifacts that can affect the identification of minerals (false positives and false negatives). Also, observational biases such as surface dust cover, ice, photometric effects, residuals in the atmospheric correc-

tion, and spectral mixing with non-hydrated minerals could affect the hydrous mineral detections from orbital data.

2. 98% of the Martian surface has not yet been observed using high resolution CRISM images. Though the multi-spectral CRISM observations cover almost the entire planet, hydrous mineral detection from multispectral CRISM data is mostly discarded by Carter et al. (2013) due to their low spectral resolution.

3. Some regions have been studied more than others, resulting in more hydrous mineral detection than in the less studied areas.

4. Small hydrous mineral exposures are covered by fewer pixels and on average have spectra with lower S/N ratios, making them harder to identify.

In addition to the limitations of the response variable (hydrous mineral detection), two other types of uncertainties and errors can be mainly identified; 1) errors and uncertainties associated with the original data or introduced during the pre-processing and processing of vector/raster data, and 2) errors and uncertainties introduced during the information representation and digital fusion of the factor maps (Moon, 1998). Since the global maps used in this study were of different resolutions, coordinate systems, and different file formats, errors and uncertainties can be introduced during the resampling process, reclassification process, projection and transformation, and data handling. These errors and uncertainties can transmit through the entire process and into the final results. Some of the errors and uncertainties are introduced during the information representation and digital fusion, and the methods used to eliminate some of these errors and uncertainties are briefly discussed below.

This study did not test the Conditional Independence (CI) among the evidential maps, though some evidential maps seem to have a conditional dependence (e.g., Albedo, Thermal inertia, dust cover index). Conditional dependence can create problems when combining maps using fuzzy algebraic product, fuzzy algebraic sum, and γ operator. However, before applying these three operators, all the similar maps were synthesized using fuzzy OR and fuzzy AND operators to eliminate the effect of Conditional Independence. Therefore, it is not necessary that conditionally dependent maps are rejected in the predictive mineral mapping process using fuzzy logic, if an appropriate inference network is used (Porwal et al., 2003). However, if extremely high or low noise values are associated with some pixels in evidential maps, the fuzzy OR and fuzzy AND operators would propagate into the final synthesized fuzzy favorability map (Knox-Robinson, 2000). These noises (no data pixels and saturated pixels) were observed in most of the used image products. If fuzzy algebraic sum (FAS) and fuzzy algebraic product (FAP) operators were used individually, these noises could be amplified because of the increasive and decreasive tendencies of these two operators, respectively. The fuzzy γ operators balanced these tendencies of the FAS and FAP operators by using appropriate values of γ (Porwal et al., 2003; Knox-Robinson, 2000). One of the main advantages of fuzzy models are

their capability to control the propagation of extreme-value noise to the output. This study continues to select the best sites (pixels) that have the highest favorability index for zeolites for detailed high resolution spectral studies.

5 Conclusions

In this study, the data-driven fuzzy based weights-of-evidence method was applied to produce a hydrous mineral favorability map and a zeolite mineral favorability map of the surface of Mars up to 40^o latitudes towards both poles. The results of this work lead to the following main conclusions:

1. The methods applied in this study dealt well with qualitative, quantitative, multi-source data/information for Mars, acquired from orbital data, which may be imprecise and incomplete due to the limitations of spatial resolution, spatial coverage, surface dust, instrumental biases, and other intrinsic biases.

2. The weights-of-evidence method provided a simple statistical method for predicting mineral potential based on limited known occurrences.

3. The most important and sensitive processes in fuzzy modeling were the definition of fuzzy membership values of multiclass evidential maps and the selection of fuzzy set operators and an appropriate inference network for combining the evidential maps.

4. The favorability map for hydrous minerals obtained by a well-tuned fuzzy inference engine indicates a strong correlation (success rate) between the areas of high favorability of hydrous minerals and known hydrous mineral detections.

5. Favorability for zeolites was derived from the favorability of hydrous mineral map and the pyroclastic deposits (modeled and confirmed) map and agrees with previous studies conducted in those favorable areas, supporting the validity of the conceptual model used and its accuracy.

6. The favorable areas for zeolites identified in this method include the eastern and western Arabia deposits and some sites in the Medusae Fossae formation within previously mapped potential pyroclastic deposits. Favorable areas for zeolites outside the mapped pyroclastic deposits include certain areas of Valles Marineris, Mawrth Vallis, highlands north of Hellas, and the Terra Cimmeria, and Terra Sirenum regions.

Acknowledgments

Many thanks to NASA, ESA and all the authors for making the image data and image derived products are available. Also, thanks to the developers of ILWIS, GDAL, ISIS3, R, and Rstudio for making them as free, and to Bas Retsios at the Faculty of ITC, the University of Twente, the Netherlands for helpful discussions on ILWIS.

Open Research

Data is available through Alemanno et al. (2018), Bandfield (2002), Boynton et al. (2004), Broz et al. (2020), Carter et al. (2013), Goudge et al. (2016), Kerber et al. (2013), Ody et al. (2012), Poulet et al. (2007), Putzig and Mellon (2007), Ruff and Christensen (2002), Smith et al. (2001), and Tanaka et al. (2014).

References

Alemanno, G., Orofino, V., Mancarella, F. (2018). Global map of Martian fluvial systems: Age and total eroded volume estimations. Earth and Space Science, 5, 560–677.

Ansan, V., Loizeau, D., Mangold, N., Le Mouélic, S., Carter, J., Poulet, F., Dromart, G., Lucas, A., Bibring, J. -P., Gendrin, A., Gondet, B., Langevin, Y., Masson, Ph., Murchie, S., Mustard, J. F., Neukum, G. (2011). Stratigraphy, mineralogy, and origin of layered deposits inside Terby Crater, Mars. Icarus, 211, 273–304.

Bandfield, J. L. (2002). Global mineral distributions on Mars. Journal of Geophysical Research. 107 (E6, 5042), 10.1029/2001JE001510.

Bandfield, J. L., Hamilton, V. E., Christensen, P. R. (2000). A global view of Martian surface compositions from MGS-TES. Science, 287 (5458), 1626–1630.

Barnhart, C. J., Nimmo, F. (2011). Role of impact excavation in distributing clays over Noachian surfaces. Journal of Geophysical Research, 116 (E01009).

Basu, A., Schmitt, J., Crossey, L. J. (1998). An argument for zeolites in Mars rocks and an Earth analog. In Proc. Lunar Planet Sci. Conf. 24th. Abstract No.1041.

Berkley, J. L., Drake, M. J. (1981). Weathering of Mars: Antarctic analog studies. Icarus, 45, 231–249.

Bibring, J-P., Soufflot, A., Berthé, M., Langevin, Y., Gondet, B., Drossart, P., Bouyé, M., Combes, M., Puget, P., Semery, A., Bellucci, G., Formisano, V., Moroz, V., Kottsov, V., Bonello, G., Erard, S., Forni, O., Gendrin, A., Manaud, N., Poulet, F., Poulleau, G., Encrenaz, T., Fouchet, T., Melchiori, R., Altieri, F., Ignatiev, N., Titov, D., Zasova, L., Coradini, A., Capacionni, F., Cerroni, P., Fonti, S., Mangold, N., Pinet, P., Schmitt, S., Sotin, C., Hauber, E., Hoffmann, H., Jaumann, R., Keller, U., Arvidson, R., Mustard, J., Forget, F. (2004). OMEGA: Observatoire Pour La Minéralogie, l'eau, Les Glaces Et l'activité. Eur. Space Agency Spec. Publ. ESA SP-1240, 37–49.

Bish, D. L., Carey, J. W., Vaniman, D. T., Chipera, S. J. (2003). Stability of hydrous minerals on the Martian surface. Icarus, 164, 96–103.

Bishop, J. L., Loizeau, D., McKeown, N. K., Saper, L., Dyar, M. D., Des Marais D. J., Parente, M., Murchie, S. L. (2013). What the ancient phyllosilicates at Mawrth Vallis can tell us about possible habitability on early Mars. Planetary and Space Science, 86, 130–149.

Bishop, Janice L., and Elizabeth B. Rampe. 2016. "Evidence for a Changing Martian Climate from the Mineralogy at Mawrth Vallis." Earth and Planetary Science Letters 448: 42–48.

Bonham-Carter, G. F., Agterberg, F. P., Wright, D. F. (1989). Weights of Evidence modelling: A new approach to mapping mineral potential. In Statistical Applications in the Earth Sciences, edited by Agterberg, F. P., Bonham-Carter, G. F., Geological Survey of Canada, 171–183.

Bonham-Carter, G. F. (1994). Geographic Information Systems for Geoscientists: Modelling with GIS. Pergamon.

Boynton, W. V., Feldman, W. C., Mitrofanov, I. G., Evans, L. G., Reedy, R. C., Squyres, S. W., Starr, R., Trombka, J. I., D'Uston, C., Arnold, J. R., Englert, P. A. J., Metzger, A. E., Wanke, H., Bruckner, J., Drake, D. M., Shinohara, C., Fellows, C., Hamara, D. K., Harshman, K., Kerry, K., Turner, C., Ward, M., Barthe, H., Fuller, K. R., Storms, S. A., Thornton, G. W., Longmire, J. L., Litvak, M. L., Ton'chev, A. K. (2004). The Mars Odyssey Gamma-ray spectrometer instrument suite. Space Science Reviews, 110, 37–83.

Boynton, W. V., Taylor, G. J., Evans, L. G., Reedy, R. C., Starr, R., Janes, D. M., Kerry, K. E., Drake, D. M., Kim, K. J., Williams, R. M. S., Crombie, M. K., Dohm, J. M., Baker, V., Metzger, A. E., Karunatillake, S., Keller, J. M., Newsom, H. E., Arnold, J. R., Bruckner, J., Englert, P. A. J., Gasnault, O., Sprague, A. L., Mitrofanov, I., Squyres, S. W., Trombka, J. I., d'Uston, L., Wanke, H., Hamara, D. K. (2007). Concentration of H, Si, Cl, K, Fe, and Th in the low- and mid-latitude regions of Mars. Journal of Geophysical Research, 112 (E12S99), doi:10.1029/2007JE002887.

Broz, P., Bernhardt, H., Conway, S. J., Parekh, R. (2020). An overview of explosive volcanism on Mars. Journal of Volcanology and Geothermal Research, 107125.

Cabrol, N. A., Grin, E. A. (1999). Distribution, classification, and ages of Martian impact crater lakes. Icarus, 142, 160–172.

Cabrol, N. A., Grin, E. A. (2002). Overview on the formation of paleolakes and ponds on Mars. Global and Planetary Changes, 35, 199–219.

Cannon, K. M., Mustard, J. F., Salvatore, M. R. (2015). Alteration of immature sedimentary rocks on Earth and Mars: Recording aqueous and surface–atmosphere processes. Earth and Planetary Science Letters, 417, 78–86.

Carr, M. H., Chuang, F. C. (1997). Martian Drainage Densities. Journal of Geophysical Research, 102 (E4), 9145–9152.

Carranza, E. J. M. (2011). Geocomputation of Mineral Exploration Targets. Computers & Geosciences, 37, 1907–1916.

Carter, J., Poulet, F., Bibring, J. -P., Mangold, N., Murchie, S. (2013). Hydrous minerals on Mars as seen by the CRISM and OMEGA imaging spectrometers:

Updated global view. Journal of Geophysical Research: Planets, 118, 831–858.

Cheng, Q., Agterberg, F. P. (1999). Fuzzy Weights of Evidence method and its application in mineral potential mapping. Natural Resources Research, 8 (1), 27–35.

Chipera, S. J., Apps, J. A. (2001). Geochemical Stability of Natural Zeolites. Reviews in Mineralogy & Geochemistry, 45 (1), 117–161.

Christensen, P. R., Bandfield, J. L., Hamilton, V. E., Ruff, S. W., Kieffer, H. H., Titus, T. N., Malin, M. C., Morris, R. V., Lane, M. D., Clark, R. L., Jakosky, B. M., Mellon, M. T., Pearl, J. C., Conrath, B. J., Smith, M. D., Clancy, R. T., Kuzmin, R. O., Roush, T., Mehall, G. L., Gorelick, N., Bender, K., Murray, K., Dason, S., Greene, E., Silverman, S., Greenfield, M. (2001). Mars Global Surveyor Thermal Emission Spectrometer experiment: Investigation description and surface science results. Journal of Geophysical Research, 106 (E10), 23, 823–23, 871.

Christensen, P. R., Anderson, D. L., Chase, S. C., Clark, R. N., Kieffer, H. H., Malin, M. C., Pearl, J. C., Carpenter, J., Bandiera, N., Brown, F. G., Silverman, S. (1992). Thermal Emission Spectrometer experiment: Mars Observer Mission. Journal of Geophysical Research, 97 (E5), 7719–7724.

Davis, J. M., Balme, M., Grindrod, P. M., Williams, R. M. E., Gupta, S. (2016). Extensive Noachian fluvial systems in Arabia Terra: Implications for early Martian climate. Geology, 44 (10), 847–850.

Davis, J. M., Gupta, S., Balme, M., Grindrod, P. M., Fawdon, P., Dickeson, Z. D., Williams, R. M. E. (2019). A diverse array of fluvial depositional systems in Arabia Terra: Evidence for mid-Noachian to early Hesperian rivers on Mars. Journal of Geophysical Research: Planets, 124, 1913–1934.

Dibble, W. E., Tiller, W. A. (1981). Kinetic model of zeolite paragenesis in tuffaceous sediments. Clays and Clay Minerals, 29 (5), 323–30.

Dickinson, W. W., Rosen, M. R. (2003). Antarctic permafrost: An analogue for water and diagenetic minerals on Mars. Geology, 31 (3), 199–202.

Ehlmann, B. L., Edwards C. S. (2014). Mineralogy of the Martian surface. Annual Review of Earth and Planetary Sciences, 42, 291–315.

Ehlmann, B. L., Mustard, J. F., Swayze, G. A., Clark, R. N., Bishop, J. L., Poulet, F., Des Marais, D. J., Roach, L. H., Milliken, R. E., Wray, J. J., Barnouin-Jha, O., Murchie, S. L. (2009). Identification of hydrated silicate minerals on Mars using MRO-CRISM: Geologic context near Nili Fossae and implications for aqueous alteration. Journal of Geophysical Research, 114 (E00D08), doi:10.1029/2009JE003339.

Evans, L. G., Squyres, S. W. (1987). Investigation of Martian H2O and CO2 via orbital Gamma Ray Spectroscopy. Journal of Geophysical Research, 92 (B9), 9153–9167.

Fassett, C. I., Head, J. W. (2007). Layered mantling deposits in Northeast Arabia Terra, Mars: Noachian-Hesperian sedimentation, erosion, and terrain inversion. Journal of Geophysical Research, 112 (E08002).

Fassett, C. I., Head, J. W. (2008). Valley network-fed, open-basin lakes on Mars: Distribution and implications for Noachian surface and subsurface hydrology. Icarus, 198, 37–56.

Goudge, T. A., Aureli, K. L., Head, J. W., Fassett, C. I., Mustard, J. F. (2015). Classification and analysis of candidate impact crater-hosted closed-basin lakes on Mars. Icarus, 260, 346–367.

Goudge, T. A., Fassett, C. I., Head, J. W., Mustard, J. F., Aureli, K. L. (2016). Insights into surface runoff on early Mars from paleolake basin morphology and stratigraphy. Geology, doi:10.1130/G37734.1.

Goudge, T. A., Head, J. W., Mustard, J. F., Fassett, C. I. (2012). An analysis of open-basin lake deposits on Mars: Evidence for the nature of associated lacustrine deposits and post-lacustrine modification processes. Icarus, 219, 211–229.

Grant, J. A., Schultz, P. H. (1990). Gradational epochs on Mars: Evidence from west-northwest of Isidis Basin and Electris. Icarus, 84, 166–195.

Hargitai, H. I., Gulick, V. C., Glines, N. H. (2018). Paleolakes of northeast Hellas: Precipitation, groundwater-fed, and fluvial lakes in the Navua–Hadriacus–Ausonia region, Mars. Astrobiology, 18 (11), 1435–1459.

Hartmann, W. K. (2005). Martian cratering 8: Isochron refinement and the chronology of Mars. Icarus, 174, 294–320.

Hay, R. L. (1966). Zeolites and zeolitic reactions in sedimentary rocks. Special GSA Papers No 85, 130.

Hay, R. L., Sheppard, R. A. (2001). Occurrence of zeolites in sedimentary rocks: An overview. In Natural Zeolites: Occurrence, Properties, Applications, edited by Bish D. L., Ming, D. Reviews in Mineralogy; Geochemistry, 45 (1),217–234.

Hynek, B. M., Beach, M., Hoke, M. R. T. (2010). Updated global map of Martian valley networks and implications for climate and hydrologic processes. Journal of Geophysical Research, 115 (E09008), doi:10.1029/2009JE003548.

Iijima, A. (1988). Chapter 3. Diagenetic transformations of minerals as exemplified by zeolites and silica minerals - a Japanese view. In Developments in Sedimentology, Diagenesis II, edited by Chilingarian, G. V., Wolf, K. H., 43,147–211.

Irwin, R. P., Howard, A. D., Craddock, R. A., Moore, J. M. (2005). An intense terminal epoch of widespread fluvial activity on early Mars: 2. Increased runoff and paleolake development. Journal of Geophysical Research, 110 (E12S15).

Kerber, L., Forget, F., Madeleine, J.-B., Wordsworth, R., Head, J. W., Wilson, L. (2013). The effect of atmospheric pressure on the dispersal of pyroclasts from Martian volcanoes. Icarus, 223, 149–156.

Kerber, L., Head, J. W. (2010). The age of the Medusae Fossae Formation: Evidence of Hesperian emplacement from crater morphology, stratigraphy, and ancient lava contacts. Icarus, 206, 669–684.

Kerber, L., Head, J. W., Madeleine, J.-B., Forget, F., Wilson, L. (2012). The dispersal of pyroclasts from ancient explosive volcanoes on Mars: Implications for the friable layered deposits. Icarus, 219, 358–381.

Knox-Robinson, C. M. (2000). Vectorial Fuzzy Logic: A novel technique for enhanced mineral perspectivity mapping, with reference to the orogenic gold mineralization potential of the Kalgoorlie Terrane, Western Australia. Australian Journal of Earth Sciences, 47, 929–941.

Lander, R. H., Hay, R. L. (1993). Hydrogeologic control on zeolitic diagenesis of the White River sequence. Geological Society of America Bulletin, 105, 361–376.

Lee, Y. I. (1988). Chemistry and origin of zeolites in sandstones at DSDP Sites 445 and 446, Daito Ridge and Basin Province, Northwest Pacific. Chemical Geology, 67, 261–273.

Loizeau, D., Werner, S. C., Mangold, N., Bibring, J.-P., Vago, J. L. (2012). Chronology of deposition and alteration in the Mawrth Vallis region, Mars. Planetary and Space Science, 72, 31–43.

Luo, W., Stepinski, T. F. (2009). Computer-generated global map of valley networks on Mars. Journal of Geophysical Research, 114 (E11010).

Luo, X., Dimitrakopoulos, R. (2003). Data-driven Fuzzy analysis in quantitative mineral resource assessment. Computers & Geosciences, 29, 3–13.

Malin, M. C., Bell, J. F., Cantor, B. A., Caplinger, M. A., Calvin, W. M., Clancy, R. T., Edgett, K. S., Edwards, L., Haberle, R. M., James, P. B., Lee, S. W., Ravine, M. A., Thomas, P. C., Wolff, M. J. (2007). Context Camera investigation on board the Mars Reconnaissance Orbiter. Journal of Geophysical Research, 112 (E05S04), doi:10.1029/2006JE002808.

Mandt, K. E., de Silva, S. L., Zimbelman, J. R., Crown, D. A. (2008). Origin of the Medusae Fossae Formation, Mars: Insights from a synoptic approach. Journal of Geophysical Research, 113 (E12011).

McEwen, A. S., Eliason, E. M., Bergstrom, J. W., Bridges, N. T., Hansen, C. J., Delamere, W. A., Grant, J. A., Gulick, V. C., Herkenhoff, K. E., Keszthelyi, L., Kirk, R. L., Mellon, M. T., Squyres, S. W., Thomas, N., Weitz, C. M. (2007). Mars Reconnaissance Orbiter's High Resolution Imaging Science Experiment (HiRISE). Journal of Geophysical Research, 112 (E05S02), doi:10.1029/2005JE002605.

McHenry, L. J., Kodikara, G. R. L., Stanistreet, I. G., Stollhofen, H., Njau, J. K., Schick, K., Toth, N. (2020). Lake conditions and detrital sources of Paleolake Olduvai, Tanzania, reconstructed using x-Ray diffraction analysis of cores. Palaeogeography, Palaeoclimatology, Palaeoecology, 556 (109855)

Mellon, M. T., Jakosky, B. M., Kieffer, H. H. (2000). High-resolution thermal inertia mapping from the Mars Global Surveyor Thermal Emission Spectrometer. Icarus, 148, 437–455.

Michalski, J. R., Niles, P. B., Cuadros, J., Baldridge, A. M. (2013). Multiple working hypotheses for the formation of compositional stratigraphy on Mars: Insights from the Mawrth Vallis region. Icarus, 226, 816–840.

Ming, D. W., Gooding, J. L. (1988). Zeolites on Mars: Possible environmental indicators in soils and sediments. In Workshop on Mars Sample Return Science, LPI Technical Report 88-07,124–125. Lunar & Planetary Institute.

Mitrofanov, I., Malakhov, A., Djachkova, M., Golovin, D., Litvak, M., Mokrousov, M., Sanin, A., Svedhem, H., Zelenyi, L. (2022). The evidence for unusually high Hydrogen abundances in the central part of Valles Marineris on Mars. Icarus 374 (114805).

Moon, W. M. (1998). Integration and fusion of geological exploration data: A theoretical review of Fuzzy Logic approach. Geoscience Journal, 2 (4), 175–183.

Moore, J. M. (1990). Nature of the mantling deposit in the heavily cratered terrain of Northeastern Arabia, Mars. Journal of Geophysical Research, 95 (B9), 14, 279–14, 289.

Neuhäuser, B., Terhorst, B. (2007). Landslide susceptibility assessment using "Weights-of-Evidence" applied to a study area at the Jurassic escarpment (SW-Germany). Geomorphology, 86 (1-2), 12–24.

Ody, A., Poulet, F., Langevin, Y., Bibring, J. -P., Bellucci, G., Altieri, F., Gondet, B., Vincendon, M., Carter, J., Manaud, N. (2012). Global maps of anhydrous minerals at the surface of Mars from OMEGA/MEx. Journal of Geophysical Research, 117 (E00J14), doi:10.1029/2012JE004117.

Osterloo, M. M., Anderson, F. S., Hamilton, V. E., Hynek, B. M. (2010). Geologic context of proposed Chloride-bearing materials on Mars. Journal of Geophysical Research, 115 (E10012), doi:10.1029/2010JE003613.

Pan, G., Harris, D. P. (2000). Information Synthesis for Mineral Exploration. Oxford University Press.

Pleskot, L. K., Miner, E. D. (1981). Time variability of Martian bolometric albedo. Icarus, 45, 179–201.

Porwal, A., Carranza, E. J. M., Hale, M. (2003). Knowledge-driven and data-driven Fuzzy models for predictive mineral potential mapping. Natural Resources Research, 12 (1), 1–25.

Poulet, F., Gomez, C., Bibring, J. -P., Langevin, Y., Gondet, B., Pinet, P., Belluci, G., Mustard, J. (2007). Martian surface mineralogy from Observatoire Pour La Mine´ralogie, l'eau, Les Glaces Et l'activite´ on board the Mars Express Spacecraft (OMEGA/MEx): Global mineral maps. Journal of Geophysical Research, 112 (E08S02), doi:10.1029/2006JE002840.

Putzig, N. E., Mellon, M. T. (2007). Apparent thermal inertia and the surface heterogeneity of Mars. Icarus, 191, 68–94.

Ramirez, R. M. (2017). A warmer and wetter solution for early Mars and the challenges with transient warming. Icarus, 297, 71–82.

Renaut, R. W. (1993). Zeolitic diagenesis of late Quaternary fluviolacustrine sediments and associated calcrete formation in the Lake Bogoria basin, Kenya Rift Valley. Sedimentology, 40, 271–301.

Romero-Calcerrada, R., and Luque, S. (2006). Habitat quality assessment using Weights-of-Evidence based GIS modelling: The case of Picoides Tridactylus as species indicator of the biodiversity value of the Finnish forest. Ecological Modelling, 196, 62–76.

Ruff, S. W., Christensen, P. R. (2002). Bright and dark regions on Mars: Particle size and mineralogical characteristics based on thermal emission spectrometer data. Journal of Geophysical Research, 107 (E12, 5127), doi:10.1029/2001JE001580.

Schumm, S. A. (1991). To interpret the Earth: Ten ways to be wrong. Cambridge University Press.

Semprich, J., Schwenzer, S. P., Treiman, A. H., Filiberto, J., 2019. Phase equilibria modeling of low-grade metamorphic Martian rocks. J. Geophys. Res. 124: 681-702.

Sheppard, R. A., Gude. A. J. (1968). Distribution and genesis of authigenic silicate minerals in tuffs of Pleistocene Lake Tecopa, Inyo County California. Geological Survey Professional Paper, United States Government Printing Office, Washington 597, 38 pp.

Sheppard, R. A., Gude, A. J., Fitzpatrick, J. J. (1988). Distribution, characterization, and genesis of mordenite in Miocene silicic tuffs at Yucca Mountain, Nye County, Nevada. U. S. Geological Survey Bulletin, 1777, 27 pp.

Smith, D. E., Zuber, M. T., Frey, H. V., Garvin, J. B., Head, J. W., Muhleman, D. O., Pettengill, G. H., Phillips, R. J., Solomon, S. C., Zwally, H. J., Banerdt, W. B., Duxbury, T. C., Golombek, M. P., Lemoine, F. G., Neumann, G. A., Rowlands, D. D., Aharonson, O., Ford, P. G., Ivanov, A. B., Johnson, C. L., McGovern, P. J., Abshire, J. B., Afzal, R. S., Sun, X. (2001). Mars Orbiter Laser Altimeter: Experiment summary after the first year of global mapping of Mars. Journal of Geophysical Research, 106 (E10), 23, 689–23, 722.

Sun, V. Z., Milliken, R. E. (2015). Ancient and recent clay formation on Mars

as revealed from a global survey of hydrous minerals in crater central peaks. Journal of Geophysical Research: Planets, 120, 2293–2332.

Tanaka, K. L., Robbins, S. J., Fortezzo, C. M., Skinner, J. A., Hare, T. M. (2014). The digital global geologic map of Mars: Chronostratigraphic ages topographic and crater morphologic characteristics, and updated resurfacing history. Planetary and Space Science, 95, 11–24.

Tanaka, K. L. (2000). Dust and ice deposition in the Martian geologic record. Icarus, 144, 254–266.

Tanaka, K. L., Skinner, J. A., Dohm, J. M., Irwin, R. P., Kolb, E. J., Fortezzo, C. M., Platz, T., Michael, G. G., Hare, T. M. (2014). Geologic map of Mars. U.S. Geological Survey Scientific Investigations Map 3292, Scale 1:20,000,000, Pamphlet, 43.

Thollot, P., Mangold, N., Ansan, V., Mouélic, S. L., Milliken, R. E., Bishop, J. L., Weitz, C. M., Roach, L. H., Mustard, J. F., Murchie, S. L. (2012). Most Mars minerals in a nutshell: Various alteration phases formed in a single environment in Noctis Labyrinthus. Journal of Geophysical Research, 117 (E00J06), doi:10.1029/2011JE004028.

Tokano, T., Bish, D. L. (2005). Hydration state and abundance of zeolites on Mars and the water cycle. Journal of Geophysical Research, 110 (E12S08), doi:10.1029/2005JE002410.

Viviano-Beck, C. E., Murchie, S. L., Beck, A. W., Dohm, J. M. (2017). Compositional and structural constraints on the geologic history of eastern Tharsis Rise, Mars. Icarus, 284, 43–58.

Wendt, L., Bishop, J. L., Neukum, G. (2013). Knob fields in the Terra Cimmeria/Terra Sirenum region of Mars: Stratigraphy, mineralogy and morphology. Icarus, 225, 200–215.

Whelley, P., Novak, A. M., Richardson, J., Bleacher, J., Mach, K., Smith, R. N. (2021). Stratigraphic evidence for early Martian explosive volcanism in Arabia Terra. Geophysical Research Letters, 48 (e2021GL094109).

Wilson, L., Head, J. W. (2007). Explosive volcanic eruptions on Mars: Tephra and accretionary lapilli formation, dispersal and recognition in the geologic record. Journal of Volcanology and Geothermal Research, 163, 83–97.

Wray, J. J., Milliken, R. E., Dundas, C. M., Swayze, G. A., Andrews-Hanna, J. C., Baldridge, A. M., Chojnacki, M., Bishop, J. L., Ehlmann, B. L., Murchie, S. L., Clark, R. N., Seelos, F. P., Tornabene, L. L., Squyres, S. W. (2011). Columbus crater and other possible groundwater-fed paleolakes of Terra Sirenum, Mars. Journal of Geophysical Research, 116 (E01001), 41.

Wray, J. J., Murchie, S. L., Bishop, J. L., Ehlmann, B. L., Milliken, R. E., Wilhelm, M. B., Seelos, K. D., Chojnacki, M. (2016). Orbital evidence for more

widespread carbonate bearing rocks on Mars. Journal of Geophysical Research: Planets, 121, 625–677.

Yang, X.-Q., Kodikara, G. R. L., Luedeling, E., Yang, X.-F., He, J., Liu, P.-g., Xu, J.-C. (2012). Looking below the ground: Prediction of Tuber Indicum habitat using the Weights of Evidence method. Ecological Modelling, 247, 27–39.

Zadeh, L. A. (1965). Fuzzy Sets. Inform. Control, 8, 338–353.

Zhao, J., Xiao, L., Goudge, T. D. (2020). Paleolakes in the northwest Hellas region, Mars: Implications for the regional geologic history and paleoclimate. Journal of Geophysical Research: Planets, 125 (e2019JE006196).

Zimmermann, H. J. (1991). Fuzzy Set Theory and Its Applications. Vol. 1. Springer.

Zimmermann, H. J., Zysno, P. (1980). Latent connectives in human decision making. Fuzzy Sets and Systems, 4, 37–51.

Zolotov, M. Y., Mironenko, M. V., 2016. Chemical Models for Martian Weathering Profiles: Insights into Formation of Layered Phyllosilicate and Sulfate Deposits. Icarus 275: 203–220.